Chapter 2
Theoretical Background

A high intensity laser pulse (>10^{18} W/cm^2) incident on a nanometer thin foil rapidly ionizes the atoms of the irradiated material and thus interacts with a solid density plasma. The ionization process sets in at comparably low intensities ($\sim 10^{13}$ W/cm^2) at the foot of the pulse, and in strong fields, is well described through tunnel or barrier suppression ionization, covered by many textbooks [1]. This chapter introduces the theoretical framework needed to understand the electron dynamics in laser plasma interactions, reviews the concept of electron mirror generation from nanoscale foils and discusses the reflection properties of relativistic electron mirror structures.

2.1 Fundamentals of Light

Electromagnetic radiation is described by Maxwell's equations [2]. The electric and magnetic fields $\boldsymbol{E}$, $\boldsymbol{B}$ can be directly found from them. Introducing the potentials $\boldsymbol{A}$, ϕ such that

$$\begin{aligned} \boldsymbol{E} &= -\nabla\phi - \tfrac{\partial}{\partial t}\boldsymbol{A} \\ \boldsymbol{B} &= \nabla \times \boldsymbol{A} \end{aligned} \tag{2.1}$$

and using the Lorenz Gauge $\nabla \boldsymbol{A} + c^{-2}\partial\phi/\partial t = 0$, Maxwell's equations reduce to the symmetric wave equations

$$\begin{aligned} \Delta\phi - \tfrac{1}{c^2}\tfrac{\partial^2}{\partial t^2}\phi &= -\rho/\epsilon_0 \\ \Delta\boldsymbol{A} - \tfrac{1}{c^2}\tfrac{\partial^2}{\partial t^2}\boldsymbol{A} &= -\mu_0 \boldsymbol{j} \end{aligned} \tag{2.2}$$

where c denotes the speed of light, ϵ_0 the electric permittivity and μ_0 magnetic permeability. In vacuum, the electric charge and current density vanish ($\boldsymbol{j} = \rho = 0$) and hence, a laser pulse is simply described by

$$\boldsymbol{A}(\boldsymbol{r}, t) = \boldsymbol{A}_{\boldsymbol{A}}(\boldsymbol{r}, t)\sin(\boldsymbol{k_L} \cdot \boldsymbol{r} - \omega_L t + \phi) \tag{2.3}$$

D. Kiefer, *Relativistic Electron Mirrors*, Springer Theses,
DOI 10.1007/978-3-319-07752-9_2

with the dispersion relation $\omega_L = ck_L$ and phase ϕ. Thus, the electric and magnetic fields are given by

$$\begin{aligned} \boldsymbol{E}(\boldsymbol{r},t) &= \boldsymbol{E_A}(\boldsymbol{r},t)\cos(\boldsymbol{k_L}\cdot\boldsymbol{r}-\omega_L t+\phi) \\ \boldsymbol{B}(\boldsymbol{r},t) &= \boldsymbol{B_A}(\boldsymbol{r},t)\cos(\boldsymbol{k_L}\cdot\boldsymbol{r}-\omega_L t+\phi) \end{aligned} \tag{2.4}$$

with envelope functions $\boldsymbol{E_A} = c\boldsymbol{B_A} = \omega_L \boldsymbol{A_A}$ and $\boldsymbol{E_A} \perp \boldsymbol{B_A}$, $\boldsymbol{E_A} \perp \boldsymbol{k_L}$, $\boldsymbol{B_A} \perp \boldsymbol{k_L}$. For a plane wave, $E_A(\boldsymbol{r},t) = E_0$, whereas for a gaussian pulse shape, the field distribution in the focal point is $E_A(\boldsymbol{r},t) = E_0\, e^{-t^2/\tau_L^2}\, e^{-(x^2+y^2)/w_0^2}$. Assuming a gaussian profile (in space and time), the peak intensity of the pulse can be determined from the laser pulse energy E, the FWHM pulse duration t_{FWHM} and the FWHM focal spot size d_{FWHM} using[1]

$$I_0 = \frac{0.82 \cdot E}{t_{FWHM}\, d_{FWHM}^2} \tag{2.5}$$

Theoretically, the intensity of the pulse can be derived from the cycle-averaged Poynting vector, thus $I_0 = \langle S\rangle_T = \epsilon_0 c^2 \langle |E \times B|\rangle_T = c\epsilon_0 E_0^2/2$. Now, if we use the normalized vector potential $\boldsymbol{a} = e\boldsymbol{A}/m_e c$ to express the electric field of the laser $E_0 = m_e c\omega_L/e \cdot a_0$ we find for the intensity

$$I_0 = \frac{1.37 \cdot 10^{18}\,\mathrm{W/cm^2}}{\lambda^2[\mu\mathrm{m}]} a_0^2 \tag{2.6}$$

Using that expression in combination with Eq. 2.5, we can deduce the a_0 parameter frequently used in theory and simulation. It is worth noting that the fields achieved with the laser pulse are simply

$$\begin{aligned} E_L &= 3.2 \cdot \tfrac{a_0}{\lambda_L[\mu\mathrm{m}]} \times 10^{12}\,\mathrm{V/m} \\ B_L &= 1.07 \cdot \tfrac{a_0}{\lambda_L[\mu\mathrm{m}]} \times 10^{4}\,\mathrm{T} \end{aligned} \tag{2.7}$$

Thus, the laser pulses used in this thesis reach electric fields in the range of tens of TV/m and magnetic fields on the order of 10^4–10^5 T.

2.2 Single Electron Motion in a Relativistic Laser Field

The interaction of an intense laser pulse with a solid density plasma is a very complex, many body system, which in general cannot be described analytically. Nonetheless, to get a better insight into the interaction dynamics, it is instructive to study the single electron motion in an electromagnetic wave, as these dynamics very often can still be recovered even in the large scale systems.

[1] $t_{FWHM} = \sqrt{2\ln 2}\tau_L$, $d_{FWHM} = \sqrt{2\ln 2} w_0$.

The equation of motion of an electron in an electromagnetic field is given by the Newton-Lorentz equation

$$\frac{d}{dt}\boldsymbol{p} = -e\,(\boldsymbol{E} + \boldsymbol{v} \times \boldsymbol{B}) \tag{2.8}$$

This set of coupled partial differential equations can by solved analytically following [3, 4]. However, a deeper understanding of the system can be gained using the Lagrangian formalism and considering fundamental symmetries [5].

2.2.1 Symmetries and Invariants

In the following, we will work in relativistic units. The normalized variables are derived from their counterparts in SI-units:

$$E \to E' = \frac{E}{m_e c^2} \qquad \Phi \to \phi' = \frac{e\,\Phi}{m_e c^2} \qquad z \to z' = k_L z$$
$$p \to p' = \frac{p}{m_e c} \qquad A \to a' = \frac{e\,A}{m_e c} \qquad t \to t' = \omega_L t$$

Note that the energy of the particle is just $E = \gamma$ with $\gamma = (1 - \boldsymbol{\beta}^2)^{-1/2} = \sqrt{1 + {p'_x}^2 + {p'_z}^2}$. For the sake of simplicity we shall neglect the $'$ in the following discussion. The relativistic Lagrangian function of an electron moving in an electromagnetic field with vector potential $\boldsymbol{A}$ and electrostatic potential ϕ reads [2, 6]

$$L = -\sqrt{1 - \boldsymbol{\beta}^2} - \boldsymbol{\beta}\boldsymbol{a} + \phi \tag{2.9}$$

from which we can derive the canonical momentum $\boldsymbol{p^{can}} = \frac{\partial L}{\partial \boldsymbol{\beta}} = \gamma\boldsymbol{\beta} - \boldsymbol{a} = \boldsymbol{p} - \boldsymbol{a}$. If we now consider potentials that are dependent on the z coordinate only, i.e. $\boldsymbol{a} = a(z,t)\,\boldsymbol{e_x}$ and $\phi = \phi(z)$, the planar symmetry of the system $\partial L/\partial x = 0$ implies that the canonical momentum in the transverse direction is conserved, that is

$$\frac{d}{dt}p_x^{can} = \frac{d}{dt}\frac{\partial L}{\partial \beta_x} = \frac{\partial L}{\partial x} = 0 \Rightarrow p_x - a = const \tag{2.10}$$

We can derive a second invariant if we neglect the electrostatic potential $\phi = 0$ and consider a wave form $a = a(t - z)$. As a result, the system is anti-symmetric in the coordinates z, t, which implies $\partial L/\partial t = -\partial L/\partial z$. Making use of the relation $dH/dt = -\partial L/\partial t$ for the Hamiltonian function, we can write

$$\frac{dH}{dt} = -\frac{\partial}{\partial t}L = \frac{\partial L}{\partial z} = \frac{d}{dt}\frac{\partial L}{\partial \beta_z} = \frac{d}{dt}p_z^{can} \tag{2.11}$$

and we find the second integral of motion ($H = \gamma$)

$$\frac{d}{dt}\left(\gamma - p_z^{can}\right) = 0 \Rightarrow \gamma - p_z^{can} = const. \tag{2.12}$$

We can now immediately solve the equations of motion making use of the integrals derived in the previous section. Conservation of the transverse canonical momentum (Eq. 2.10) yields $p_x^{can}(t) = p_x^{can}(t_0) = \alpha_0$, hence

$$p_x(t) = \alpha_0 + a(t) \tag{2.13}$$

As for a plane wave $a_z = 0$, thus $p_z^{can} = p_z$, we define the constant of motion $\kappa_0 = (\gamma - p_z)\,|_{t=t_0}$ and obtain from the second invariant (Eq. 2.12)

$$\gamma(t) = \kappa_0 + p_z(t) \tag{2.14}$$

which in combination with $\gamma = \sqrt{1 + p_x^2 + p_z^2}$ gives

$$p_z(t) = \frac{1}{2\kappa_0}\left(1 - \kappa_0^2 + p_x^2(t)\right) \tag{2.15}$$

Now, if we consider a plane wave with electric field $e_L = -a_0 \cos(\tau + \phi_0)$ and vector potential $a = a_0 \sin(\tau + \phi_0)$, where $\tau = t - z$, we immediately find for the momenta

$$\begin{aligned} p_x(\tau) &= \gamma\beta_\perp = a_0 \sin(\tau + \phi_0) + \alpha_0 \\ p_z(\tau) &= \gamma\beta_z = \tfrac{1}{2\kappa_0}\left(1 - \kappa_0^2 + [a_0 \sin(\tau + \phi_0) + \alpha_0]^2\right) \\ \gamma(\tau) &= \kappa_0 + \tfrac{1}{2\kappa_0}\left(1 - \kappa_0^2 + [a_0 \sin(\tau + \phi_0) + \alpha_0]^2\right) \end{aligned} \tag{2.16}$$

where the constants of motion α_0, κ_0 can be determined from the initial conditions $p_{z,0}, p_{x,0}, \phi_0$

$$\alpha_0 = p_{x,0} - a_0 \sin\phi_0 \qquad \kappa_0 = \gamma_0 - p_{z,0} \qquad \gamma_0 = \sqrt{1 + p_{\perp,0}^2 + p_{z,0}^2} \tag{2.17}$$

To obtain the electron trajectory, we make use of a change in variables which considerably simplifies the integration of Eq. 2.16. Using $\tau = t - z$ as independent variable implies $d\tau = (1 - \beta_z)\,dt = \kappa_0/\gamma\,dt$,[2] thus substitution gives $dz/d\tau = \gamma/\kappa_0\, dz/dt = p_z/\kappa_0$ and $dx/d\tau = \gamma/\kappa_0\, dx/dt = p_x/\kappa_0$, which can be integrated

[2] $(1 - \beta_z) = (\gamma - p_z)/\gamma = \kappa_0/\gamma$, using Eq. (2.14).

$$
\begin{aligned}
t &= z + \tau \\
x(\tau) &= \frac{1}{\kappa_0}\left[\alpha_0 \tau - a_0\left(\cos\left(\tau + \phi_0\right) - \cos\phi_0\right)\right] \\
z(\tau) &= \frac{1}{\kappa_0^2}\left[\left(1 + \alpha_0^2 - \kappa_0^2 + \frac{a_0^2}{2}\right)\frac{\tau}{2} - a_0\left(\alpha_0 \cos\left(\tau + \phi_0\right) + \frac{a_0}{8}\sin\left(2\left(\tau + \phi_0\right)\right)\right)\right. \\
&\quad \left. + a_0\left(\alpha_0 \cos\phi_0 + \frac{a_0}{8}\sin 2\phi_0\right)\right]
\end{aligned}
\tag{2.18}
$$

It is worth noting that for an electron initially at rest ($p_{z,0} = p_{x,0} = 0$), Eqs. 2.13–2.15 simplify considerably, as in this case

$$
\begin{aligned}
p_x(t) &= a(t) - a(t_0) \\
p_z(t) &= \tfrac{1}{2} p_x^2(t) \\
\gamma(t) &= 1 + p_z(t)
\end{aligned}
\tag{2.19}
$$

Hence, the kinetic energy is just $E_{kin} = (\gamma - 1) = p_x^2/2$, which reveals that the energy gain of the particle stems from the transverse electric field, whereas the $v \times B$ term turns the particle quiver motion into the forward direction without adding energy to it.

Figure 2.1 depicts the electron dynamics of an electron initially at rest. The particle motion is strongly dependent on the initial phase, which crucially governs the maximal energy achieved in the field $\gamma^{max} = 1 + \frac{a_0^2}{2}(1 + \sin\phi_0)^2$. Moreover, depending on the initial phase, the electron oscillates in transverse dimension with amplitude $x^{max} = a_0$ or gradually drifts in either one direction (Fig. 2.1d).

2.2.2 Single Electron Motion in a Finite Pulse

The solution derived so far is strictly speaking only valid for infinite plane waves. Imposing a more realistic temporally finite, gaussian shaped pulse the equations of motion cannot be solved analytically anymore and numerical methods (here: Fourth Order Runge-Kutta) need to be used. Figure 2.2 shows the numerical integration of an electron propagating in a gaussian shaped, finite pulse. The kinetic energy of the electron is directly coupled to the light field and returns back to zero as soon as the (slightly slower propagating) electron is overtaken by the laser pulse. This is a direct consequence of the conservation of the transverse canonical momentum (Eq. 2.10). Since initially $p_x(t = -\infty) = a(t = -\infty) = 0$ the final transverse momentum is $p_x(t = \infty) = a(t = \infty) = 0$ and likewise $p_z = p_x^2/2 = 0$, which means that a charged particle cannot gain energy from a plane wave in vacuum. It needs the break up of symmetry for effective energy gain.

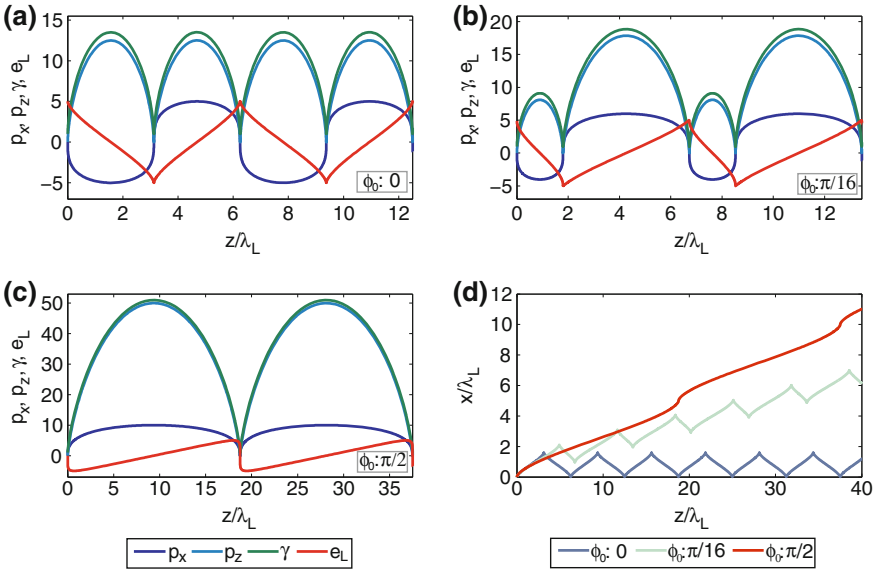

Fig. 2.1 *Single electron motion in a plane wave*. Depending on the injection phase ϕ_0, the electron is accelerated (decelerated) within one quarter ($\phi_0 = 0$) to one half cycle ($\phi_0 = \pi/2$) of the driving field ($a_0 = 5$). Note the different scales of the abscissa and ordinate axis. **a**–**c** depict the electron slippage over 2 laser cycles, **d** shows the corresponding electron motion in space

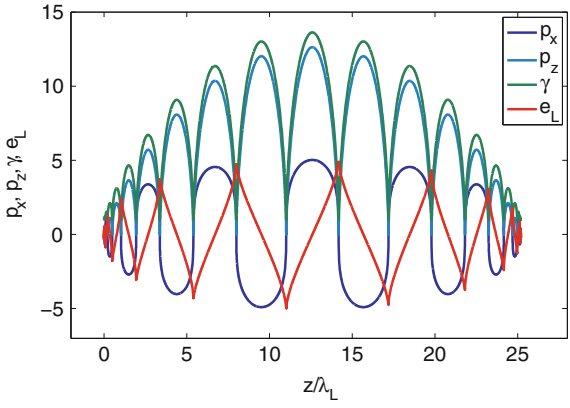

Fig. 2.2 *Single electron in a finite pulse*. Gaussian pulse shape ($a_0 = 5$, $\tau_{FWHM} = 10$ fs)

2.2.3 The Lawson Woodward Principle and Its Limitations

The fundamental question under what conditions a free electron can extract energy from an electromagnetic laser field has been a controversial debate over many years. General starting point is the so called Lawson-Woodward Theorem [7, 8], which

states that the net energy gain of an isolated relativistic electron interacting with an electromagnetic field is zero. However, the proof of this theorem is bound to a number of assumptions [1, 9, 10]

- the laser field is in vacuum with no walls or boundaries present,
- the electron is ultra-relativistic along the acceleration path,
- no static electric or magnetic fields are present,
- the interaction region is infinite,
- nonlinear effects can be neglected.

Here, it should be noted that the Lorentz force $\boldsymbol{v} \times \boldsymbol{B}$ is linear in the ultra-relativistic case ($v \to c$) and does not violate the Lawson-Woodward Principle. Despite the vast number of underlying assumptions, this theorem has proven its relevance over the years and was recently confirmed in a test experiment [11].

Nonetheless, numerous acceleration schemes have been developed in theory violating one or many of the underlying conditions in order to accelerate electrons in vacuum effectively. In the following, we will highlight only a few aspects of those schemes relevant for this work.

2.2.4 Acceleration in an Asymmetric Pulse

Breaking up symmetry in time and assuming that we could find a mechanism that could inject electrons right into the middle of a pulse at time t_0, the situation completely changes and a non-zero energy gain can be extracted from the electromagnetic field [4, 12]. Using Eq. 2.19, we find for the final energy of the electron

$$\gamma^{final} = 1 + \frac{1}{2}(a(\infty) - a(t_0))^2 = 1 + \frac{1}{2}a(t_0)^2 \tag{2.20}$$

Thus, the energy gain strongly depends on the phase of the field at the injection time t_0. Approximating the vector potential of a gaussian pulse with $a \approx a_0 \exp(-t^2/\tau_L^2) \sin\phi(t, x)$ (adiabatic approximation) and taking into account that the electric field is $e_L = -\partial a/\partial t$, we find maximum energy gain for $\phi(t, x) = \pi/2$ corresponding to $e_L \propto \cos(\pi/2) = 0$. Hence, electrons injected into the field at the zero points close to the peak of the pulse experience substantial energy gain from the electromagnetic field as can be seen in Fig. 2.3.

A scheme that could potentially seed electrons right into the peak of the pulse is to exploit the ionization dynamics of highly charged ions [13, 14]. As it was shown in simulation, inner shell electrons of high Z atoms remain during the rise time of the laser pulse and are released from the ionic core (and thus injected right into the maximal intensity region) when the pulse reaches its peak intensity. Recently, it was pointed out that the laser nanofoil interaction might exhibit similar dynamics, which could provide effective means of accelerating electrons from semi-transparent solid plasmas and which will be discussed in great detail in Chap. 4.

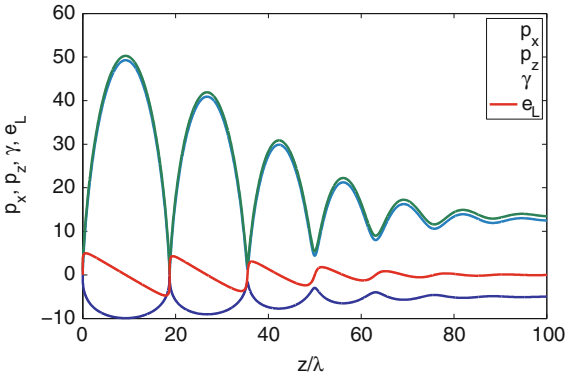

Fig. 2.3 *Single electron in an asymmetric pulse*. The electron is injected into the laser field at the peak of the pulse with $p_{x,0} = p_{z,0} = 0$ and $\phi_0 = \pi/2$. Same pulse as in Fig. 2.2

2.2.5 Ponderomotive Scattering

To reach high intensities, laser pulses are focused tightly to within a few μm only and thus the field distribution interacting with the electron in experiment is strongly dependent on its radial position. While for a plane wave, the cycle-averaged Lorentz force acting on the particle turns out to be zero,[3] inhomogeneous fields exhibit a nonzero component, which causes the particle to drift from high intensity to low intensity regions. The origin of the ponderomotive force can be easily understood if we consider a particle initially located at the center of the focal spot. Owing to the transverse electric field, the electron is displaced from its central position to regions of lowered intensities. Thus, as the oscillating field changes sign the force driving the electron back to the center is smaller and therefore, the electron does not return to its initial position. As a result, the oscillation center gradually drifts from regions of high intensity to those of lower intensity while the mean kinetic energy of the particle successively increases with every cycle.

This phenomenon is well known at sub-relativistic intensities and can be derived from first order perturbation analysis of the Lorentz force around the oscillation center [1].[4] In the relativistic regime, the longitudinal motion has to be taken into account. Assuming that the particle motion can be separated into $\boldsymbol{p} = \bar{\boldsymbol{p}} + \tilde{\boldsymbol{p}}$ where $\bar{\boldsymbol{p}}$ and $\tilde{\boldsymbol{p}}$ denote the slowly varying and the rapidly varying part with respect to the laser frequency, the generalized, relativistic ponderomotive force reads [15, 16]

$$\boldsymbol{F_p} = -\frac{m_e c^2}{4\bar{\gamma}} \nabla \boldsymbol{a_A}^2 \qquad \bar{\gamma} = \sqrt{1 + \bar{p}_z^2 + \bar{p}_\perp^2 + a_A^2/2} \tag{2.21}$$

[3] $F \propto p/\gamma \cdot B \propto \sin\tau \cos\tau \propto \sin 2\tau$, thus $\langle F \rangle_\tau = 0$.

[4] At sub-relativistic intensities, the ponderomotive potential of the laser field is $\Phi_p = \frac{e^2 E_A^2}{4 m_e \omega_L^2} = \frac{m_e c^2}{4} a_A^2$ and the ponderomotive force is just simply $F_p = -\nabla \Phi_p = -\frac{m_e c^2}{4} \nabla a_A^2$.

The main feature still applies: The electron drifts away from the high intensity region owing to the gradient of the intensity distribution and eventually scatters out of the focused beam—thus, overall gaining energy from the electromagnetic field of the laser (Fig. 2.4). While this process was observed in experiment at rather low intensities, accelerating electrons up to few hundred keVs and scattering angles in excellent agreement with those expected from single electron dynamics [17, 18], the ponderomotive scattering in the high intensity regime [19, 20], which is expect to occur when the electron quiver amplitude ($x = a_0$) reaches the length scale of the beam waist at the focus has been discussed quite controversial [16, 21]. In particular, it was shown that a rather simple treatment of the electromagnetic field distribution in the focal plane using the paraxial Gaussian beam approximation [19] fails considerably in predicting the final energy gain and angular distribution [16, 22]. Including higher order corrections, especially longitudinal fields, the final energy gain is found to be significantly reduced, the scattering angle turns out to be highly dependent on the initial position and is no longer limited to the polarization plane only. Taking into account that the actual focal distribution of test particle studies is rather difficult.

Figure 2.4 illustrates the ponderomotive scattering of an electron in a Gaussian mode (lowest order approximation) clearly showing the effective energy gain of an electron from a finite field distribution in space. Longitudinal field components appear in the next order [16] which may play an important role. A correct field distribution up to all orders is given in [16, 22], nonetheless, this may still be different from the actual experimental conditions.

In conclusion, we find that the dynamics of a single electron injected into a relativistic, tightly focused laser pulse is very complex with strong dependence on the exact field distribution in the focal region and the initial position of the electron.

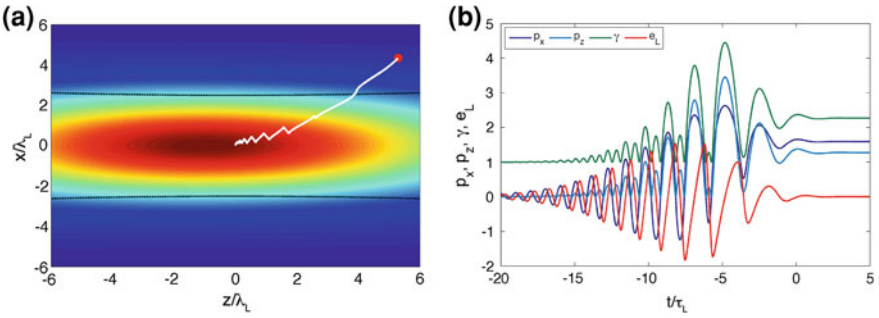

Fig. 2.4 *Ponderomotive scattering*. Single electron in a finite, Gaussian shaped pulse with beam waist $w_0 = 2\,\mu$m and pulse duration $\tau_{FWHM} = 10$ fs. **a** Electron trajectory (*white line*) and instantaneous position (*red dot*) at $t/\tau_L = -1.1$ superimposed with a snapshot of the cycle-averaged intensity distribution at that moment in time. **b** Temporal evolution of the electron energy and momentum

2.2.6 Vacuum Acceleration Schemes

While in the case of ponderomotive scattering, electrons are quickly expelled from the focused laser beam, certain regions surrounding the laser axis have been identified where high energetic electrons can be trapped and accelerated for a long time [23–25]. Detailed analysis of the diffracting laser beam reveals that in these sectors the effective phase velocity of the laser field is slightly smaller than the speed of light. Hence, relativistic electrons injected into these regions are quasi-phase-matched with the accelerating field and thus experience a drastic energy gain. Although it was argued that the so-called electron capture and acceleration scenario (CAS) even works for electrons initially at rest when accounting for the longitudinal field components of the focal spot [22], the mechanism requires rather high intensities $a_0 \sim 10$–100, is critically dependent on the exact field distribution and thus still remains experimentally unexplored.

While in the high intensity regime, electrons initially at rest interacting with a tightly focused beam tend to be scattered transversally long before the peak of the pulse has reached, it was argued that a ring-like intensity profile would focus the accelerating particles towards the beam axis, owing to the off-axis potential well originating from the intensity distribution [26, 27].

2.3 Laser Propagation in a Plasma

We now turn our discussion from single particle interactions to a dense plasma. Here, we shall briefly introduce the fundamental properties of a cold plasma, meaning that we essentially neglect forces arising from the thermal pressure of the plasma. Derivations are given in many textbooks [1, 5, 28].

In a neutral plasma, electrons displaced from their equilibrium position feel a restoring force caused by the positive ion background and thus oscillate with the plasma frequency

$$\omega_p = \sqrt{\frac{n_e e^2}{\epsilon_0 m_e \bar{\gamma}}} \tag{2.22}$$

where $\bar{\gamma}$ is the cycle-averaged Lorentz factor in the plasma, often set to $\bar{\gamma} = \sqrt{1 + a_0^2/2}$. It is worth noting that due to their much higher mass, ions stay quasi immobile on the time scale of the plasma frequency and thus can be viewed as a uniform background in this context. From the dispersion relation of an electromagnetic wave propagating in a plasma,

$$\omega_L^2 = \omega_p^2 + c^2 k_L^2 \tag{2.23}$$

we can derive the refractive index $n_R = c/v_{ph}$

$$n_R = \sqrt{1 - \frac{\omega_p^2}{\omega_L^2}} \tag{2.24}$$

Thus, in the case of a rather low density plasma ($\omega_p < \omega_L$), light propagates with phase velocity $v_{ph} = c/n_R$ and group velocity $v_g = cn_R$. However, if $\omega_p > \omega_L$, the refractive index becomes imaginary. In this case, the response of the plasma electrons is much faster than the frequency of the electromagnetic wave and therefore the incident wave is effectively shielded at every moment in time in the plasma. Depending on the electron density, the plasma can either be overdense (opaque) or underdense (transparent) to the incident light field. The interaction dynamics are fundamentally different in these two scenarios and we define the critical density at which $\omega_p = \omega_L$, to distinguish those two regimes. Using Eq. 2.22, we find for the critical density

$$n_c = \frac{\epsilon_0 m_e}{e^2} \bar{\gamma}\, \omega_L^2 = \bar{\gamma} \cdot \frac{1.1 \cdot 10^{21}}{\lambda[\mu\mathrm{m}]^2} \mathrm{cm}^{-3} \tag{2.25}$$

Hence, an electromagnetic wave incident on an overdense plasma reflects from the plasma surface where it interacts as an evanescent wave within the skin layer of the plasma. For a step-like boundary, we can define the characteristic length scale over which the electric field drops to $1/e$, i.e. the plasma skin depth as

$$l_s = \frac{c}{\sqrt{\omega_p^2 - \omega_L^2}} \approx \frac{c}{\omega_p} \tag{2.26}$$

2.3.1 Laser Interaction with an Overdense Plasma

A laser pulse normally incident on an overdense plasma is reflected and thus interacts as a standing wave with the critical surface of the plasma. At relativistic intensities, the $v \times B$ component of the resultant electromagnetic field drives the plasma surface in longitudinal direction with

$$F_z = F_0 \left(1 - \cos 2\omega_L t\right) \tag{2.27}$$

which oscillates at twice the frequency of the incident laser field.[5] Note, that the driving force does not change sign and thus on time average pushes the critical surface into the plasma, whereas the oscillating high frequency component eventually leads

[5] this rather general expression is readily derived from the ponderomotive force when including the fast oscillating component [29], or alternatively from a perturbative model [30]. A more detailed theoretical treatment is given in [31] using a one particle plasma model, which has proven good agreement with PIC simulations.

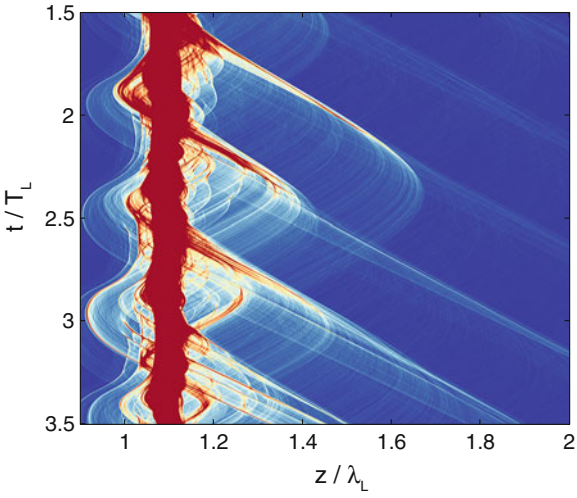

Fig. 2.5 *Electron bunch generation at the laser-plasma boundary*. At every laser (half-)cycle, a group of electrons is accelerated to MeV energies and injected as a dense bunch into the plasma

to strong electron heating. At oblique incidence, the situation is quite similar. Here, the leading term driving the critical surface is the electric field component pointing normal to the plasma boundary, which however oscillates at a frequency of ω_L, only, and acts in both directions. In both cases, the interplay between the driving force and the restoring charge separation field leads to the oscillation of the plasma surface at the frequency of the driving force. This collective motion of the electrons at the plasma boundary can be modeled analytically [31] and is the key component for the generation of high harmonics from solids in the relativistic regime.

Along with the oscillatory surface motion, at every half (full) cycle, a group of electrons acquires high energies at the laser plasma boundary and is injected as a dense bunch into the overdense region (Fig. 2.5). As the laser field does not penetrate into the plasma interior, these electrons immediately escape from the driving laser field with energies on the order of several MeVs well above the bulk electron plasma temperature.

The periodic formation of these high energetic electron bunches at a sharp laser plasma boundary is evident in simulations and has been confirmed experimentally probing the optical transition radiation emitted from the generated hot electron current crossing the rear surface of the target. Here, the optical emission spectra were found to be spiked at ω_L and $2\omega_L$, which hints that these bunches preserve their temporal periodicity to some extend as they propagate through the plasma [32, 33]. In the vacuum region behind the target, the expelled electron bunches quickly disperse in the electrostatic sheath field built up during the interaction and eventually form a hot electron cloud surrounding the target rear side, which in turn causes the acceleration of ions.

Although initially highly confined in space, the generated electron bunches are spectrally very broadband. Moreover, the energy distribution of subsequent bunches fluctuates from cycle to cycle and the overall, time-integrated electron spectra

observed in experiment and simulation resemble exponentially decaying distribution functions, with characteristic slope commonly referred to as the hot electron temperature. As it was pointed out by Bezzerides et al. [34], the spectral shape is a direct consequence of the stochastic nature of the bunch formation process, as theoretically, the integration over many bunches with random variations in the energy spectrum eventually leads to a Maxwellian distribution.

While exponential, hot electron distributions have been measured over decades in laser plasma experiments [1, 35–39], the physical mechanism of the electron bunch formation at the vacuum plasma interface is still not understood. Recently, a deeper insight into the process was given by Mulser et al. [40] who showed that this phenomenon may be explained by an anharmonic resonance in the attractive charge separation potential at the plasma vacuum boundary. Here, electrons with large oscillation amplitude may be driven into resonance thereby break up with the collective plasma motion and rapidly gain energy from the laser. Yet, owing to the stochastic nature of this process, no theory exists to date, which could for a given set of parameters make a prediction on the electron number within a bunch or anticipate its energy distribution.

Instead, numerous scalings have been developed predicting the slope of the time-integrated hot electron distribution [41–44]. In the case of a normal incident laser pulse, [41] showed that the hot electron temperature can be related to the ponderomotive energy of the laser pulse

$$k_B T_{hot}^{Wilks} = m_e c^2 \left(\sqrt{1 + a_0^2/2} - 1 \right) \tag{2.28}$$

This scaling is intriguingly simple and experimental configurations showing fairly good agreement with the ponderomotive scaling were reported [45]. However, a more recent theoretical study [44] showed that the ponderomotive scaling is actually only valid at sub-relativistic intensities, whereas the scaling increasingly overestimates the hot electron temperatures at intensities clearly beyond the relativistic threshold ($a_0 \gg 1$).Using that the average kinetic energy of an electron ensemble can be obtained by averaging the single electron energy with respect to the phase, they find

$$k_B T_{hot}^{Kluge} = m_e c^2 \left(\frac{\pi a_0}{2 \log 16 + 2 \log a_0} - 1 \right) \tag{2.29}$$

Yet, this scaling does not account for plasma properties and is only valid for step-like density profiles. On the contrary, numerical studies indicate that the plasma density and gradient do play an important role [46, 47]. In particular, it was found that shallow plasma gradients can result in increased electron temperatures.

Closely related to the hot electron generation is the vigorously discussed question of laser energy absorption in overdense plasmas. The generation of hot electrons is a prominent example of coupling laser energy into a plasma, and very often is thought to be the dominant absorption channel. Many different mechanisms eventually lead to the generation of high energetic electrons [1, 28]. At relativistic intensities and

steep plasmas gradients, the most dominant absorption processes are $j \times B$ *heating* [29] and *Brunel* or *vacuum heating* [48]. Both processes are physically very similar. In the case of oblique incidence, electrons are driven in the electric field of the laser giving rise to the generation of MeV electron bunches at a frequency of ω_L whereas in the case of normal incidence the magnetic term of the Lorentz force dominates and repetitively generates hot electrons at a frequency of $2\omega_L$ (see discussion above). In experiment, both mechanisms most likely contribute to the measured electron distributions, as even under normal incidence the critical surface deforms during the interaction and eventually results in oblique incidence angle at the side wings of the interaction volume. Owing to the vast variety of competing absorption mechanisms, it is difficult to isolate and study a particular process in experiment. Instead, many processes very often contribute to the recorded electron data making the correct interpretation very complex. As of to date, no comprehensive theory exists and thus the physical understanding of laser absorption still remains somewhat unclear.

2.3.2 Relativistic Electron Mirrors from Nanometer Foils

The interaction of an intense laser pulse with solid density plasma has been envisioned as a way to generate relativistic attosecond electron bunches with densities close to solid [49]. In particular, numerous theoretical work has been devoted very recently to the laser–nanofoil interaction at intensities high enough to achieve complete separation of all electrons from the ions using foil thicknesses of only a few nm [50].

Figure 2.6 illustrates the interaction dynamics in this regime, showing a step-like laser pulse with $a_0 = 48$ incident on an ultrathin (effectively 4 nm) foil. The laser pulse acts like a snowplow, drives out all electrons coherently as a single dense electron layer co-moving with the laser field, whereas the ions rest at their initial position owing to their high inertia. The created electron bunch gains energy as it surfs on the electromagnetic wave of the laser and essentially acts as a superparticle following single electron dynamics. Moreover, as the laser field prevails over the electrostatic fields of the plasma, the electron bunch keeps its initial thickness and density over several laser cycles while being accelerated.

To achieve full charge separation, the electric field of the laser has to exceed the electrostatic field arising from the complete separation of all electrons from the ions. Assuming a top-hat laser pulse and a step-like plasma profile with thickness d, we can estimate when the radiation pressure exceeds the electrostatic field pressure such that no force balance can be reached

$$\frac{I}{c} \gg \frac{1}{2}\epsilon_0 E_{es}^2 \tag{2.30}$$

The electrostatic field simply is $E_{es} = en_e d/\epsilon_0$ in the case of complete charge separation. Using Eq. 2.22 and expressing the laser field in normalized units $a_0 =$

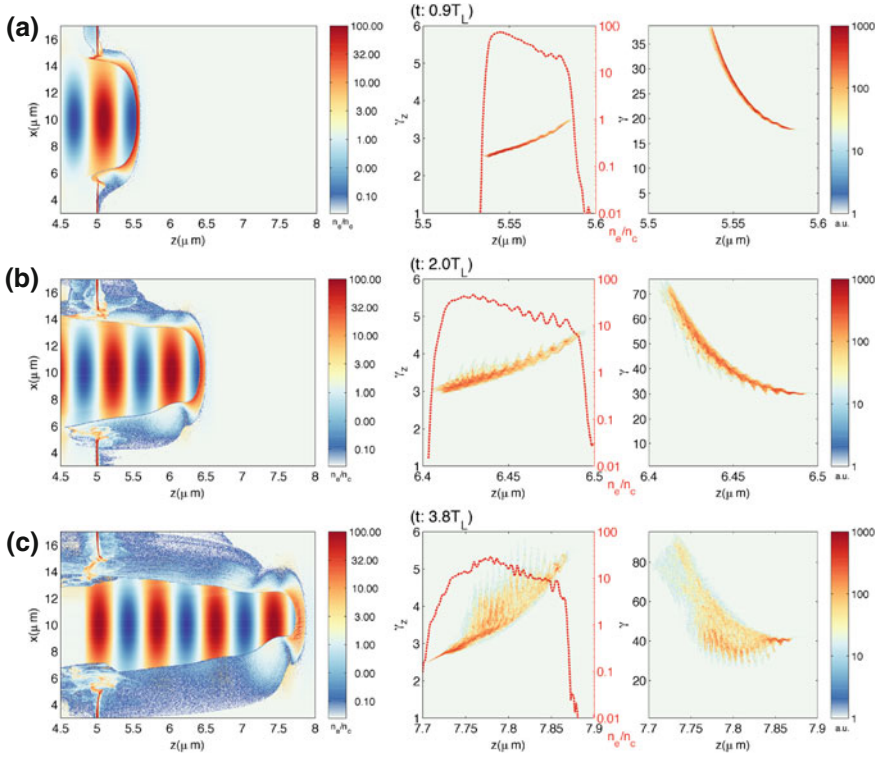

Fig. 2.6 *Laser-driven, relativistic electron mirror from a nanometer foil*. Input parameter: $a_0 = 48.3$ (pulse shape: supergaussian), $Nk_Ld = 15.7$ ($N = 100n_c$). Here, $t = 0$ is defined as the timestep when the laser pulse reaches the plasma layer. **a**–**c** depict different time steps

$eE_0/mc\omega_L$, we can rewrite the electron blowout condition as

$$a_0 \gg \frac{n_e}{n_c} k_L d \tag{2.31}$$

It is worth noting that this condition implies $d/l_s \ll a_0/\sqrt{N}$ with $N = n_e/n_c \gg 1$. Hence, in order to drive out all electrons effectively, the plasma thickness should not be much larger than the skin depth of the laser. Thus, in this scenario, the laser interacts with an overcritical, yet, transparent plasma layer.

This regime was first described by Kulagin et al. [50] and has been investigated in numerous theoretical studies since then [3, 51–53].[6] However, most of this theoretical work relies on highly idealized laser pulses with infinitely steep rise time. Using more realistic pulses with Gaussian rise spanning over many laser cycles [54, 55],

[6] Using a flattop laser pulse profile, the generation of a relativistic electron mirror was studied in great detail in [51] and an empirical lower threshold value $a_{th} = 0.9 + 1.3\,Nk_Ld$ was derived from PIC simulations. However, this threshold amplitude is strongly dependent on the temporal laser

the laser nanofoil interaction becomes very complex and yet is very little understood. Advancing this knowledge is the ambition of this thesis.

2.4 Relativistic Doppler Effect

The change in frequency and amplitude of an electromagnetic wave caused by the relative motion of the source and observer was first discussed by Einstein in his work on special relativity [56]. In his paper, Einstein calculates the reflection of an electromagnetic wave from a relativistically fast moving mirror as a working example of Lorentz transformations. The underlying idea is to transform the problem to the rest frame of the mirror, where the reflection of a light wave is well described by basic laws of optics. In the following, we shall briefly repeat Einstein's discussion here, as the result will be an integral part of this thesis.

Let the mirror propagate in $+z$ direction with velocity $\beta = v/c$ and the electromagnetic wave in $-z$ direction with wavevector $k_i = -\omega_L/c$, as shown in Fig. 2.7. As a first step, we transform the incident electromagnetic wave to the rest frame of the mirror making use of the Lorentz boost [2].

$$\begin{aligned} \omega_L'/c &= \gamma\omega_L/c - \gamma\beta k_i = (1+\beta)\gamma\omega_L/c \\ k_i' &= -\gamma\beta\omega_L/c - \gamma k_i = (1+\beta)\gamma k_i \end{aligned}$$

Thus, the incident laser field is blue shifted in the rest frame of the mirror. For the sake of simplicity, we assume a perfect mirror, which reflects back the incident field with $k_r' = -k_i'$. Now, the lab frame moves with $-\beta$ with respect to the rest frame of the mirror. Transforming the reflected light field back to the lab frame, we find

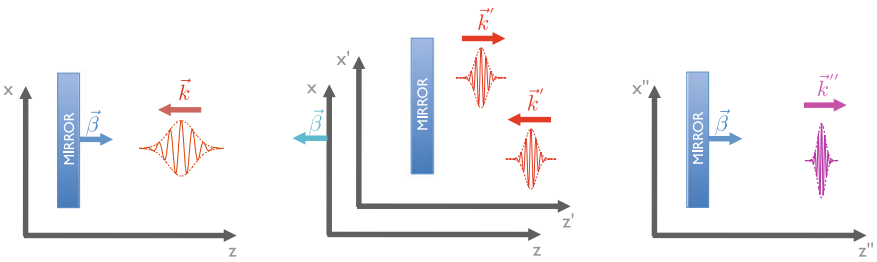

Fig. 2.7 *Relativistic Doppler effect*. Illustration of the Lorentz transformations applied to the system to discuss the reflection of a laser pulse from a counter-propagating mirror, moving with relativistic velocity β

(Footnote 6 continued)
pulse shape that is employed and might be very different for a more realistic few cycle laser pulses with Gaussian rise.

$$\omega_L''/c = \gamma\omega_L'/c - \gamma(-\beta)k_r' = (1+\beta)\gamma\omega_L'/c$$
$$k_r'' = -\gamma(-\beta)\omega_L'/c - \gamma k_r' = (1+\beta)\gamma k_r'$$

Using both equations, we find the prominent result for the reflection of an electromagnetic wave from a moving mirror:

$$\omega_L'' = (1+\beta)^2\gamma^2\omega_L \approx 4\gamma^2\omega_L$$
$$k_r'' = (1+\beta)^2\gamma^2 k_i \approx 4\gamma^2 k_i \tag{2.32}$$

Apart from the relativistic frequency upshift derived here, the amplitude and the duration of the incident wave are changed accordingly as

$$E'' = (1+\beta)^2\gamma^2 E \tag{2.33}$$

and

$$\tau'' = \frac{\tau}{(1+\beta)^2\gamma^2} \tag{2.34}$$

Equation 2.33 is obtained from the Lorentz transformation of the electromagnetic field tensor [2]. The pulse compression (Eq. 2.34) stems from the fact that the phase is an invariant under Lorentz transformations [2].

Thus, for an ideal relativistic mirror, the peak power of the reflected radiation can substantially exceed that of the incident radiation due to the increase in photon energy and accompanying temporal compression.

While theoretically extremely rewarding, the generation of a relativistic structure, with properties sufficient to act as a mirror, is extremely challenging. While electron bunches with very high γ factors can be generated with conventional accelerators, they do not form a reflecting structure analogous to a mirror due to their low density and long bunch duration and therefore the backscattered radiation is incoherent. On the contrary, the interaction of a high intensity laser pulse with a few nanometer thin free-standing foil promises the creation of a solid density, attosecond short electron bunch, which may give access to the coherent regime. In the next sections, we shall develop a deeper, microscopic understanding of the mirror properties of such a unique structure.

2.5 Coherent Thomson Scattering

Light, incident on a charged particle, such as an electron, causes the particle to be accelerated, which in turn emits radiation at the same frequency as the incident

electromagnetic wave.[7] This process is referred to as Thomson scattering with cross section $\sigma_T = 6.65 \times 10^{-25}\,\mathrm{cm}^2$ [2].

While the reflection from a mirror is usually discussed quantitatively in the framework of electrodynamics, we shall briefly analyze the reflection process from the perspective of scattering theory, as this directly highlights the main challenges to create a mirror-like structure. In scattering theory, the reflection process is a macroscopic manifestation of scattering occurring on a microscopic level. In that sense, the process is very complex as it requires the coherent behavior of a great number of individual scatterers.

In general, a mirror structure constitutes of a large ensemble of individual scatterers re-emitting light at the interface of two media with a constant phase relation, imposed via the incident light field.

Reflection, i.e. coherent scattering takes place, when many scatterers reside in a volume λ'^3, that is $n'_e\lambda'^3 \gg 1$ [57], where λ' is the wavelength of the incident light and n'_e the electron density, both values evaluated in the rest frame of the mirror.

In this scenario, the distance between adjacent scatterers is significantly shorter than the wavelength of the emitted radiation, thus the relative phases of the interfering wavelets of individual scatterers have to be taken into account to evaluate the resulting field. We shall analyze this in depth in the next section, making use of the formalisms commonly used in scattering theory.

2.5.1 Analytical Model

We start from the Thomson scattering of a single electron. The cross section is defined in such a way that the scattered power is $P_T = \sigma_T I_i$, where I_i is the incident energy flux, i.e. intensity. For an electron bunch, consisting of N scattering electrons, we can deduce the radiated power by summing over the scattering amplitudes of each individual electron while taking into account the relative phase. In general, the spatial phase factor of two scatterers separated by a distance $\mathbf{r}$ is $\phi = \mathbf{q} \cdot \mathbf{r}$, where $\mathbf{q}$ is the momentum transfer or scattering vector [58]. Considering an electron bunch with cross section A, the power incident on the bunch is $P_i = AI_i$. Thus, we can write for the backscattered power

$$P_T = \frac{\sigma_T}{A} \left| \sum_{j=1}^{N} e^{i\mathbf{q}\cdot\mathbf{r_j}} \right|^2 P_i \tag{2.35}$$

The evaluation of this sum is well established in the theory of coherent synchrotron or terahertz radiation [59, 60]. We adapt this method and write

[7] This is true as long as $\hbar\omega \ll m_e c^2$, i.e. as long as the photon recoil $\hbar\omega/c \ll m_e c$ is negligible. Otherwise, the process is described in the framework of Compton scattering.

$$P_T = \frac{\sigma_T}{A}[N[1 - f(\mathbf{q})] + N^2 f(\mathbf{q})]P_i \tag{2.36}$$

where the form factor

$$f(\mathbf{q}) = \left| \int e^{i\mathbf{q}\cdot\mathbf{r}} S(\mathbf{r}) d^3 r \right|^2 \tag{2.37}$$

is the square amplitude of the Fourier transform of the normalized particle distribution function $S(r)$, thus owing to the normalization $f(\mathbf{q}) \leq 1$.

The first term of Eq. 2.36 scales with N and describes the incoherent Thomson scattering, whereas the second term, scaling with N^2 represents the coherent contribution. As N is a large number, typically denoting 10^6–10^8 electrons, the coherent signal enhancement $Nf(k)$ can be huge, making the Thomson scattering in the coherent regime highly efficient.

In the following, we are interested in the coherent signal and define a coherent, or mirror-like reflectivity of the bunch as

$$R_m = \frac{\sigma_T}{A} N^2 f(\mathbf{q}) \tag{2.38}$$

Suppose, the electron bunch density can be modeled as a gaussian with $n_e(z) = n_0 e^{-z^2/d^2}$. Then, the number of electrons contributing to the coherent signal is $N = A \int n_e(z) dz = \sqrt{\pi} A n_0 d$ and we can construct

$$S(z) = \frac{1}{N} A\, n_e(z) = \frac{1}{\sqrt{\pi} d} e^{-z^2/d^2} \tag{2.39}$$

In the backscattering geometry $\mathbf{q} = 2k_L \mathbf{e_z}$ and we find for the form factor of an electron bunch with gaussian bunch shape

$$f(\mathbf{q} = \mathbf{2k_L}) = \left| \int e^{i2k_L z} S(z) dz \right|^2 = e^{-2k^2 d^2} \tag{2.40}$$

Thus, we write for the reflectivity of the electron mirror at rest

$$R_m = \frac{\sigma_T}{A} N^2 e^{-2k^2 d^2} \tag{2.41}$$

Now, considering a mirror moving with relativistic velocity, we transform to the rest frame of the mirror and make use of the previous discussion. In the rest frame of the mirror, the incident light is blue-shifted $k'_L = (1 + \beta)\gamma k_L$ and the electron bunch thickness becomes $d' = \gamma d$. Thus, the mirror reflectivity in the lab frame reads as

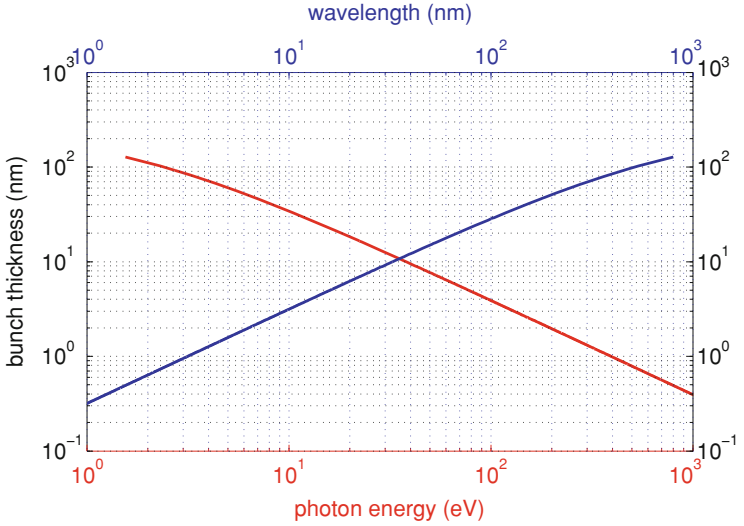

Fig. 2.8 *Dependence of the optimal electron bunch thickness on the upshifted radiation*. Here, the electron bunch thickness is defined by the FWHM value of a gaussian bunch distribution and should not be much larger than $d_{opt} = 1/2k_L\gamma^2$ as the reflectivity rapidly decreases for larger values

$$R_m = \sigma_T \pi A n_0^2 d^2 e^{-2\xi^2}$$
$$\text{with } \xi = (1+\beta)\gamma^2 k_L d \tag{2.42}$$

This formula describes the coherent backscattering from a N electron system. Note, that the coherent enhancement was discussed only in the longitudinal dimension. Thus, the cross-section A in this equation is limited to small values such that the overall quasi-one dimensional geometry of the system is preserved. In more detail, radiation with path length difference of $\Delta > \lambda_r/2$ should not contribute to the coherent enhancement in zeroth order. Thus, an electron located at a distance a from the center, contributes to the signal on axis at a distance R only if $\Delta \sim a^2/R \ll \lambda_r$. In the following, we set $a \sim \lambda_r$, thus $A = \pi\lambda_r^2$.

As an important result of the discussion, we can now define an upper limit on the electron bunch thickness d. Obviously, in order to achieve high reflectivity of the mirror structure $\xi \lesssim 1$, thus

$$k_L d_{opt} \lesssim 1/2\gamma^2. \tag{2.43}$$

It is important to note that not only the length scale (Fig. 2.8), but also the exact shape of the electron distribution is crucial for the bunch reflectivity. Figure 2.9 illustrates that fact by showing the form factor for different bunch shapes and thicknesses. As expected, the form factor drops off more rapidly for shorter wavelengths when increasing the bunch thickness while keeping the bunch shape as a gaussian. However,

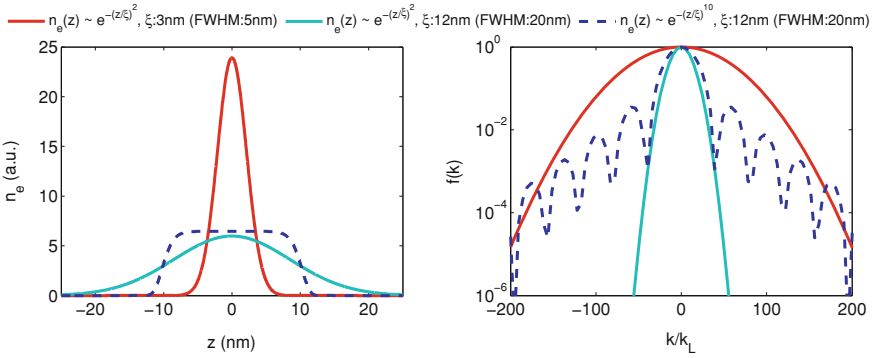

Fig. 2.9 *Dependence of the electron bunch form factor on the electron bunch shape*. The input distribution functions are normalized such that $\int n_e(z)dz = 1$

changing the bunch profile to a steeper, supergaussian profile while keeping the bunch thickness the same, does significantly reduce the fast decay of the form factor for shorter wavelengths. In essence, a mirror structure requires both high density and a sharp mirror to vacuum interface. This implies very steep density gradients, as the length scale of the discontinuity defining the mirror surface needs to be abrupt, well below the wavelength of the emitted light as the backscattered amplitudes would rather cancel out each other in a gradual changing interface [61].

2.5.2 Reflection Coefficients

We can define different reflection coefficients in the case of a moving mirror:

1. the ratio of incident and reflected power

$$R_I = \frac{I_r}{I_i} = (1+\beta)^4\gamma^4 R_m \tag{2.44}$$

2. the ratio of incident and reflected energy, corresponding to the mirror reflectivity of an ordinary mirror

$$R_E = \frac{E_r}{E_i} = \frac{I_r\tau_r}{I_i\tau_i} = (1+\beta)^2\gamma^2 R_m \tag{2.45}$$

   where the underlying assumption is that the mirror lifetime is long compared to the duration of the incident pulse.
3. The ratio of the incident and reflected photon number

$$R_{Phot} = \frac{N_r}{N_i} = \frac{E_r/\hbar\omega_r}{E_i/\hbar\omega_i} = R_E\frac{\omega_i}{\omega_r} = R_m \tag{2.46}$$

2.6 Frequency Upshift from Laser-Driven Relativistic Electron Mirrors

Inherent to the electron motion in a laser field, forward momentum is bound to a transverse momentum, thus each individual electron of the bunch propagates at an angle with respect to the laser axis of the driving laser pulse.

A counter-propagating pulse, incident on such an electron bunch causes each particle to emit dipole radiation.[8] However, as the radiating electron moves at relativistic velocity the emission cone of the radiated field is bent towards the propagation direction of the electron. In consequence, the main contribution of the incoherent signal points off-axis, along the velocity vector $\boldsymbol{\beta}$, as shown in Fig. 2.10.

In contrast, the signal of the coherent scattering is governed by the collective emission of all electrons, which is determined by the interference of the individual backscattered wavelets. Just as in an ordinary reflection, the angle of emission crucially depends in that case on the exact reflection geometry, that is the surface orientation of the scattering structure in connection with the angle of incidence of the impinging laser field and is discussed for arbitrary configurations in [53, 57]. In the counter-propagating geometry, the coherent backscatter signal adds up constructively in mirror surface normal direction, that is in the specular direction, as one would expect intuitively. In contrast, the incoherent signal, points off-axis in bunch velocity direction (Fig. 2.10), and is suppressed by destructive interference. Thus, in the case of coherent backscattering, the frequency upshift is

$$\omega_L'' = (1 + \beta_z)^2 \gamma_z^2 \omega_L \tag{2.47}$$

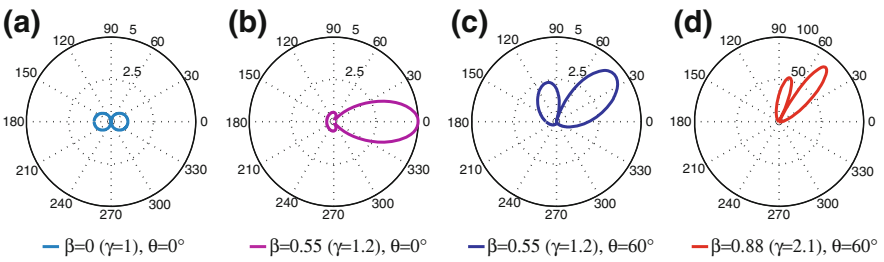

Fig. 2.10 *Dipole emission from a single electron.* Angular dependence of the emitted dipole radiation of an electron propagating with relativistic velocities β in different directions θ, **a–d**

[8] The electric field emitted from a moving charge is (consider field contributions scaling with R^{-1} only):

$$E = \frac{e}{4\pi\epsilon_0 c}\left(\frac{\boldsymbol{n} \times [(\boldsymbol{n} - \boldsymbol{\beta}) \times \dot{\boldsymbol{\beta}}]}{R(1 - \boldsymbol{n} \cdot \boldsymbol{\beta})^3}\right).$$

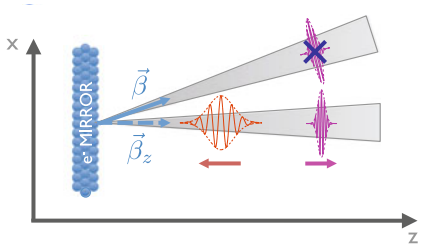

Fig. 2.11 *Relativistic Doppler upshift from laser-driven electron mirrors*. The incoherent signal points close to the direction of $\boldsymbol{\beta}$ and is fully suppressed by destructive interference in the case of a mirror-like reflection. In contrast, the coherent signal is emitted in the direction of specular reflection. Thus, the corresponding velocity component β_z governs the relativistic Doppler upshift $\sim 4\gamma_z^2$

where γ_z is the effect γ factor of the mirror motion in mirror normal direction[9] (Fig. 2.11)

$$\gamma_z = \frac{1}{\sqrt{1-\beta_z^2}} = \frac{\gamma}{\sqrt{1+(p_\perp/mc)^2}}. \tag{2.48}$$

As $p_\perp$ tends to be large due to the transverse field character of the driving laser pulse, γ_z can be significantly smaller than the full γ factor.

References

1. Gibbon P (2005) Short pulse laser interactions with matter: an introduction. Imperial College Press, London
2. Jackson JD (1998) Classical electrodynamics, 3rd edn. Wiley, New York
3. Meyer-ter Vehn J, Wu H-C (2009) Coherent thomson backscattering from laser-driven relativistic ultra-thin electron layers. Eur Phys J D: At Mol Opt Plasma Phys 55:433–441
4. Popov KI (2009) Laser based acceleration of charged particles. PhD thesis, University of Alberta
5. Meyer-ter Vehn J, Pukhov A Relativistic laser plasma interaction: analytical tools. Lecture Notes
6. Landau LD, Lifshitz EM (1980) The classical theory of fields, 4th edn. Course of theoretical physics series, vol 2. Butterworth-Heinemann, Oxford
7. Lawson JD (1979) Lasers and accelerators. IEEE Trans Nucl Sci 26(3):4217–4219
8. Woodward PM (1947) A method of calculating the field over a plane. J Inst Electr Eng 93:1554–1558
9. Palmer RB (1987) An introduction to acceleration mechanisms. SLAC-PUB-4320
10. Esarey E, Sprangle P, Krall J (1995) Laser acceleration of electrons in vacuum. Phys Rev E 52(5):5443–5453

[9] $\gamma^2 = 1 + (p_z/m_e c)^2 + (p_\perp/m_e c)^2 = 1 + (\gamma\beta_z)^2 + (p_\perp/m_e c)^2 \Rightarrow 1 + (p_\perp/m_e c)^2 = \gamma^2(1-\beta_z^2) = \gamma^2\gamma_z^{-2}$.

11. Plettner T, Byer RL, Colby E, Cowan B, Sears CMS, Spencer JE, Siemann RH (2005) Visible-laser acceleration of relativistic electrons in a semi-infinite vacuum. Phys Rev Lett 95(13):134801
12. Dodin IY, Fisch NJ (2003) Relativistic electron acceleration in focused laser fields after above-threshold ionization. Phys Rev E 68:056402
13. Hu SX, Starace AF (2002) Gev electrons from ultraintense laser interaction with highly charged ions. Phys Rev Lett 88(24):245003
14. Hu SX, Starace AF (2006) Laser acceleration of electrons to giga-electron-volt energies using highly charged ions. Phys Rev E 73(6):066502
15. Bauer D, Mulser P, Steeb WH (1995) Relativistic ponderomotive force, uphill acceleration, and transition to chaos. Phys Rev Lett 75(25):4622–4625
16. Quesnel B, Mora P (1998) Theory and simulation of the interaction of ultraintense laser pulses with electrons in vacuum. Phys Rev E 58(3):3719–3732
17. Moore CI, Knauer JP, Meyerhofer DD (1995) Observation of the transition from Thomson to Compton scattering in multiphoton interactions with low-energy electrons. Phys Rev Lett 74(13):2439–2442
18. Meyerhofer DD (1997) High-intensity-laser-electron scattering. IEEE J Quantum Electron 33(11):1935–1941
19. Hartemann FV, Fochs SN, Le Sage GP, Luhmann NC, Woodworth JG, Perry MD, Chen YJ, Kerman AK (1995) Nonlinear ponderomotive scattering of relativistic electrons by an intense laser field at focus. Phys Rev E 51(5):4833–4843
20. Malka G, Lefebvre E, Miquel JL (1997) Experimental observation of electrons accelerated in vacuum to relativistic energies by a high-intensity laser. Phys Rev Lett 78(17):3314–3317
21. McDonald Kirk T (1998) Comment on "experimental observation of electrons accelerated in vacuum to relativistic energies by a high-intensity laser". Phys Rev Lett 80(6):1350
22. Popov KI, Bychenkov VY, Rozmus W, Sydora RD (2008) Electron vacuum acceleration by a tightly focused laser pulse. Phys Plasmas 15(1):013108
23. Wang PX, Ho YK, Yuan XQ, Kong Q, Cao N, Sessler AM, Esarey E, Nishida Y (2001) Vacuum electron acceleration by an intense laser. Appl Phys Lett 78(15):2253–2255
24. Wang PX, Ho YK, Yuan XQ, Kong Q, Cao N, Shao L, Sessler AM, Esarey E, Moshkovich E, Nishida Y, Yugami N, Ito H, Wang JX, Scheid S (2002) Characteristics of laser-driven electron acceleration in vacuum. J Appl Phys 91(2):856–866
25. Pang J, Ho YK, Yuan XQ, Cao N, Kong Q, Wang PX, Shao L, Esarey EH, Sessler AM (2002) Subluminous phase velocity of a focused laser beam and vacuum laser acceleration. Phys Rev E 66(6):066501
26. Chaloupka JL, Meyerhofer DD (1999) Observation of electron trapping in an intense laser beam. Phys Rev Lett 83(22):4538–4541
27. Stupakov GV, Zolotorev MS (2001) Ponderomotive laser acceleration and focusing in vacuum for generation of attosecond electron bunches. Phys Rev Lett 86(23):5274–5277
28. Kruer WL (2003) The physics of laser plasma interactions. Westview Press, Boulder
29. Kruer WL, Estabrook K (1985) J x b heating by very intense laser light. Phys Fluids 28(1):430–432
30. Macchi A (2011) An introduction to ultraintense laser-plasma interactions
31. Rykovanov SG (20029) Interaction of intense laser pulses with overdense plasmas. Theoretical and numerical study. PhD thesis, Ludwig-Maximilians-Universität München (LMU)
32. Baton SD, Santos JJ, Amiranoff F, Popescu H, Gremillet L, Koenig M, Martinolli E, Guilbaud O, Rousseaux C, Rabec Le Gloahec M, Hall T, Batani D, Perelli E, Scianitti F, Cowan TE (2003) Evidence of ultrashort electron bunches in laser-plasma interactions at relativistic intensities. Phys Rev Lett 91:105001
33. Zheng J, Tanaka KA, Sato T, Yabuuchi T, Kurahashi T, Kitagawa Y, Kodama R, Norimatsu T, Yamanaka T (2004) Study of hot electrons by measurement of optical emission from the rear surface of a metallic foil irradiated with ultraintense laser pulse. Phys Rev Lett 92:165001
34. Bezzerides B, Gitomer SJ, Forslund DW (1980) Randomness, maxwellian distributions, and resonance absorption. Phys Rev Lett 44:651–654

35. Gitomer SJ, Jones RD, Begay F, Ehler AW, Kephart JF, Kristal R (1986) Fast ions and hot electrons in the laser-plasma interaction. Phys Fluids 29(8):2679–2688
36. Beg FN, Bell AR, Dangor AE, Danson CN, Fews AP, Glinsky ME, Hammel BA, Lee P, Norreys PA, Tatarakis M (1997) A study of picosecond laser-solid interactions up to 10[sup 19] w cm[sup - 2]. Phys Plasmas 4(2):447–457
37. Antici P, Fuchs J, Borghesi M, Gremillet L, Grismayer T, Sentoku Y, d'Humières E, Cecchetti CA, Mančić A, Pipahl AC, Toncian T, Willi O, Mora P, Audebert P (2008) Hot and cold electron dynamics following high-intensity laser matter interaction. Phys Rev Lett 101(10):105004
38. Chen H, Wilks SC, Kruer WL, Patel PK, Shepherd R (2009) Hot electron energy distributions from ultraintense laser solid interactions. Phys Plasmas 16(2):020705
39. Tanimoto T, Nishiuchi M, Mishima Y, Kikuyama K, Morioka T, Morita K, Kanasaki M, Pirozhkov AS, Yogo A, Ogura K, Fukuda Y, Sakaki H, Sagisaka A, Habara H, Tanaka KA, Kondo K (2012) Electron energy transport in the thin foil driven by high contrast high intensity laser pulse. AIP Conf Proc 1465(1):148–151
40. Mulser P, Bauer D, Ruhl H (2008) Collisionless laser-energy conversion by anharmonic resonance. Phys Rev Lett 101:225002
41. Wilks SC, Kruer WL, Tabak M, Langdon AB (1992) Absorption of ultra-intense laser pulses. Phys Rev Lett 69(9):1383–1386
42. Sherlock M (2009) Universal scaling of the electron distribution function in one-dimensional simulations of relativistic laser-plasma interactions. Phys Plasmas 16(10):103101
43. Haines MG, Wei MS, Beg FN, Stephens RB (2009) Hot-electron temperature and laser-light absorption in fast ignition. Phys Rev Lett 102(4):045008
44. Kluge T, Cowan T, Debus A, Schramm U, Zeil K, Bussmann M (2011) Electron temperature scaling in laser interaction with solids. Phys Rev Lett 107:205003
45. Malka G, Miquel JL (1996) Experimental confirmation of ponderomotive-force electrons produced by an ultrarelativistic laser pulse on a solid target. Phys Rev Lett 77(1):75–78
46. Lefebvre E, Bonnaud G (1997) Nonlinear electron heating in ultrahigh-intensity-laser-plasma interaction. Phys Rev E 55(1):1011–1014
47. Kemp AJ, Sentoku Y, Tabak M (2008) Hot-electron energy coupling in ultraintense laser-matter interaction. Phys Rev Lett 101(7):075004
48. Brunel F (1987) Not-so-resonant, resonant absorption. Phys Rev Lett 59(1):52–55
49. Naumova N, Sokolov I, Nees J, Maksimchuk A, Yanovsky V, Mourou G (2004) Attosecond electron bunches. Phys Rev Lett 93(19):195003
50. Kulagin VV, Cherepenin VA, Hur MS, Suk H (2007) Theoretical investigation of controlled generation of a dense attosecond relativistic electron bunch from the interaction of an ultrashort laser pulse with a nanofilm. Phys Rev Lett 99(12):124801
51. Kulagin VV, Cherepenin VA, Gulyaev YV, Kornienko VN, Pae KH, Valuev VV, Lee J, Suk H (2009) Characteristics of relativistic electron mirrors generated by an ultrashort nonadiabatic laser pulse from a nanofilm. Phys Rev E 80(1):016404
52. Qiao B, Zepf M, Borghesi M, Dromey B, Geissler M (2009) Coherent x-ray production via pulse reflection from laser-driven dense electron sheets. New J Phys 11(10):103042 (11pp)
53. Habs D, Hegelich M, Schreiber J, Gross M, Henig A, Kiefer D, Jung D (2008) Dense laser-driven electron sheets as relativistic mirrors for coherent production of brilliant x-ray and γ-ray beams. Appl Phys B: Lasers Opt 93:349–354
54. Tian Y, Yu W, Lu P, Xu H (2008) Generation of periodic ultrashort electron bunches and strongly asymmetric ion coulomb explosion in nanometer foils interacting with ultra-intense laser pulse. Phys Plasmas 15(5):053105
55. Popov KI, Bychenkov VY, Rozmus W, Sydora RD, Bulanov SS (2009) Vacuum electron acceleration by tightly focused laser pulses with nanoscale targets. Phys Plasmas 16(5):053106
56. Einstein A (2005) Zur Elektrodynamik bewegter Körper [AdP 17, 891 (1905)]. Ann Phys 14(S1):194–224
57. Wu H-C, Meyer-ter Vehn J (2009) The reflectivity of relativistic ultra-thin electron layers. Eur Phys J D: At Mol Opt Plasma Phys 55:443–449
58. Als-Nielsen J, McMorrow D (2001) Elements of modern X-ray physics. Wiley, New York

59. Hirschmugl CJ, Sagurton M, Williams GP (1991) Multiparticle coherence calculations for synchrotron-radiation emission. Phys Rev A 44:1316–1320
60. Carr GL, Martin MC, McKinney WR, Jordan K, Neil GR, Williams GP (2002) High-power terahertz radiation from relativistic electrons. Nature 420(6912):153–156
61. Hecht E (2001) Optics, 4th edn. Addison Wesley, Reading

http://www.springer.com/978-3-319-07751-2

Relativistic Electron Mirrors
from High Intensity Laser-Nanofoil Interactions
Kiefer, D.
2015, XIII, 117 p. 62 illus., 59 illus. in color., Hardcover
ISBN: 978-3-319-07751-2